Solution structure and metal-ion binding of the P4 element from bacterial RNase P RNA

MICHAEL SCHMITZ and IGNACIO TINOCO, JR.

Department of Chemistry, University of California, and Physical Biosciences Division,
Lawrence Berkeley National Laboratory, Berkeley, California 94720-1460, USA

ABSTRACT

We determined the solution structure of two 27-nt RNA hairpins and their complexes with cobalt(III)-hexammine $(Co(NH_3)_6^{3+})$ by NMR spectroscopy. The RNA hairpins used in this study are the P4 region from *Escherichia coli* RNase P RNA and a C-to-U mutant that confers altered divalent metal-ion specificity (Ca^{2+} replaces Mg^{2+}) for catalytic activity of this ribozyme. $Co(NH_3)_6^{3+}$ is a useful spectroscopic probe for $Mg(H_2O)_6^{2+}$-binding sites because both complexes have octahedral symmetry and have similar radii. The thermodynamics of binding to both RNA hairpins was studied using chemical shift changes upon titration with Mg^{2+}, Ca^{2+}, and $Co(NH_3)_6^{3+}$. We found that the equilibrium binding constants for each of the metal ions was essentially unchanged when the P4 model RNA hairpin was mutated, although the NMR structures show that the RNA hairpins adopt different conformations. In the C-to-U mutant a C•G base pair is replaced by U•G, and the conserved bulged uridine in the P4 wild-type stem shifts in the 3′ direction by 1 nt. Intermolecular NOE cross-peaks between $Co(NH_3)_6^{3+}$ and RNA protons were used to locate the site of $Co(NH_3)_6^{3+}$ binding to both RNA hairpins. The metal ion binds in the major groove near a bulge loop, but is shifted 5′ by more than 1 bp in the mutant. The change of the metal-ion binding site provides a possible explanation for changes in catalytic activity of the mutant RNase P in the presence of Ca^{2+}.

Keywords: ion binding; NMR; RNase P

INTRODUCTION

RNase P

RNase P is a ribonucleoprotein enzyme that catalyzes the processing of the 5′ end of tRNA in prokaryotes and eukaryotes (for reviews, see Pace & Brown, 1995; Harris et al., 1998). The RNA component of RNase P is essential for binding and positioning the precursor tRNA for catalysis; the bacterial RNase P RNA is catalytically competent without the protein component of the enzyme (Guerrier-Takada et al., 1983). Catalysis is dependent on specific divalent metal ions (Guerrier-Takada et al., 1986). The protein component of RNase P is required for stabilization of the RNA component, and may contribute to binding of required divalent metal ions. In the case of eukaryal and archaeal RNase P, one or more protein components are required for catalysis (Pace & Brown, 1995).

RNAse P structure model

Based on phylogenetic comparison of a large number of RNase P RNA sequences, chemical and enzymatic structure probing, and site-specific UV crosslinking data, the secondary structure of RNase P RNA has been established and tertiary structure models have been proposed for the bacterial RNase P RNA (Harris et al., 1994; Chen et al., 1998; Massire et al., 1998). The RNase P RNA adopts a highly base paired structure, as shown in Figure 1. Several long-range interactions, including the P4 pseudoknot and base triples between hairpin loop nucleotides and the minor groove of stem P8, result in a compact tertiary fold.

P4 element

One element of the RNase P RNA secondary structure (Fig. 1, top panel) was found to be strictly conserved among all bacterial RNase P RNAs, with clear homologs appearing also in archaeal and eukaryal P RNA. This so-called P4 element with the flanking J3/4 and J2/4 single-stranded regions occupies a central posi-
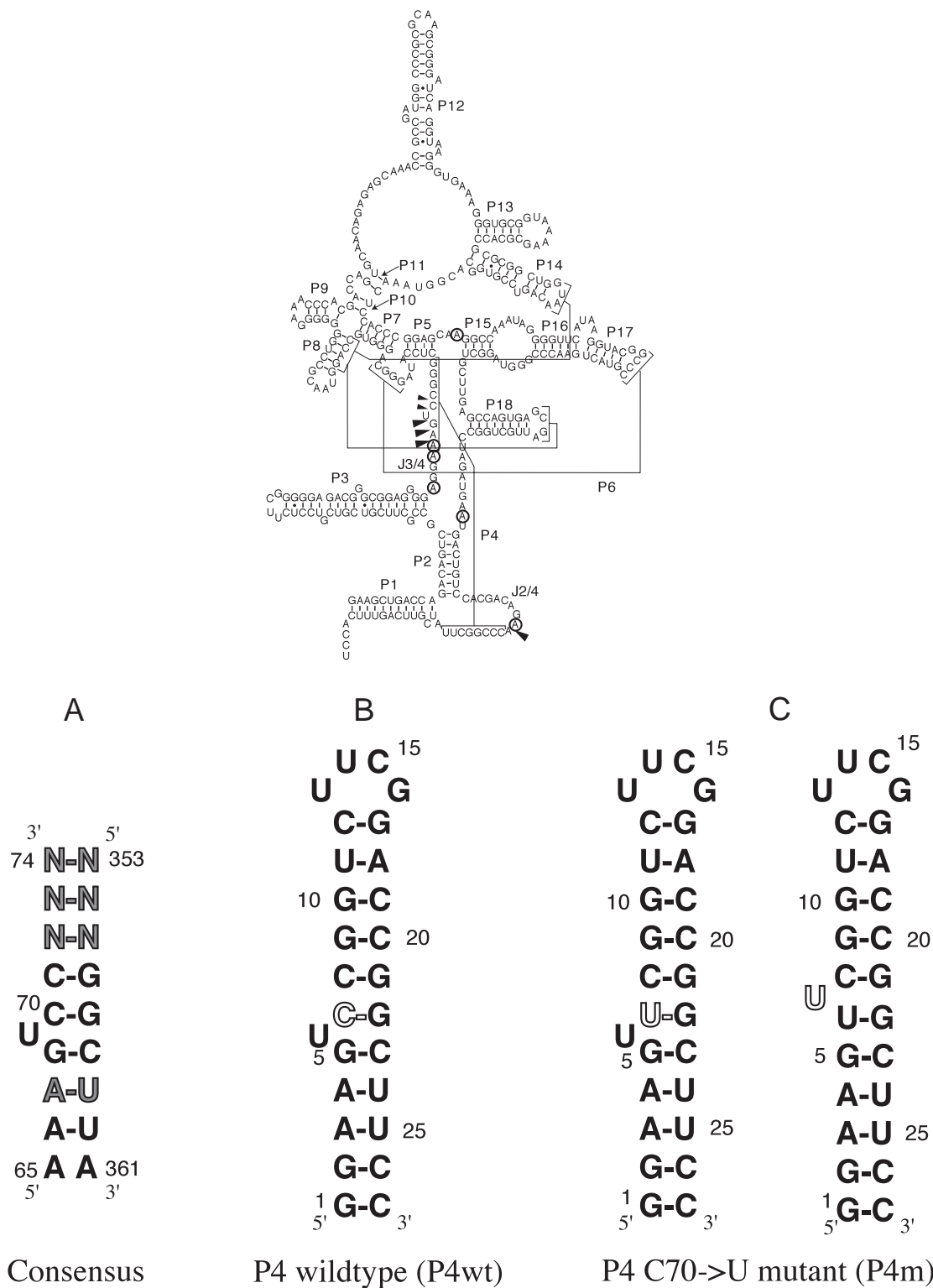
FIGURE 1. Top panel: Secondary structure of *Escherichia coli* RNase P RNA. Arrows indicate sites of phosphorothioate-modification interference and circles indicate sites of 7-deazaadenine interference (Kanzatsev & Pace, 1998). The long range interactions forming P4, P6, and two tetraloop-stem interactions are indicated by square brackets. Figure modified from Kanzatsev and Pace (1998). Bottom panel: Sequence and secondary structures of the RNA molecules used in this study. **A**: Secondary structure of the P4 element of *E. coli* RNase P RNA. The nucleotide numbering is adapted from the bacterial consensus structure. Nucleotides not strictly conserved are shown shaded. **B**: Secondary structure of the wild-type P4 element. The nucleotide C70 next to the conserved bulge uridine is shown in outline. **C**: Secondary structure of the C70 → U mutant P4 element. The mutation C70 → U next to the conserved bulge uridine is shown in outline. The two secondary structures shown are predicted to be equally stable by free-energy minimization algorithms. Only the right hand structure was observed in solution by our NMR determination of structure, however.

tion in the RNase P RNA secondary structure. The P4 element is part of a pseudoknot structure and is positioned at the center of the catalytic domain immediately adjacent to the site of the pre-tRNA cleavage according to the tertiary structure models. Binding of magnesium ions to phosphates at both ends of the P4 helix as well as to phosphates in the adjacent J2/4 and J3/4 regions has been concluded earlier from phosphorothioate modification interference studies (Harris & Pace, 1995; Hardt et al., 1996).

The very high degree of conservation, especially among bacterial sequences observed in phylogenetic studies, plus extensive mutation experiments suggest a critical role for the P4 element in catalysis. Selection for functional bacterial RNase P RNA from a pool of molecules with a randomized P4 region (Frank et al., 1996) restored the wild-type sequence as the only functional sequence, establishing the P4 region as a crucial component of the catalytic site. Selection for catalytically active RNase P RNA from randomized P4 sequences done in the presence of Ca^{2+} as a replacement for Mg^{2+} (Frank & Pace, 1997) did result in a single C-to-U base change adjacent to the bulged uridine in the P4 region (Fig. 1). Specificity for Ca^{2+} as opposed to Mg^{2+} as the catalytic metal ion was improved approximately 90-fold by this mutation. This increase in Ca^{2+} specificity was the result of a 4-fold increase of the cleavage rate in the presence of Ca^{2+} combined with a more than 20-fold decrease of the cleavage rate in the presence of Mg^{2+}. Binding affinities for Ca^{2+} are essentially the same for wild-type and mutant sequence, whereas the binding affinity for Mg^{2+} is reduced more than 10-fold in the mutant as determined by kinetic analysis of the cleavage reaction (Frank & Pace, 1997). Mg^{2+} and Ca^{2+} differ both in ionic radius and coordination geometry. The ionic radius of Ca^{2+} is 1.12 Å, 1.6-fold higher than the ionic radius of Mg^{2+}. Ca^{2+} is present as an octahydrate in aqueous solution, in contrast to the hexahydrated Mg^{2+}. These different properties of Ca^{2+} raise the possibility of a different binding site, or binding mode, for catalysis by the mutant in the presence of Ca^{2+}.

Using NMR spectroscopic techniques we investigated the structures, and the Mg^{2+} and Ca^{2+} binding to both the isolated wild-type (P4wt, Fig. 1) and mutant P4 element (P4m, Fig. 1). $Co(NH_3)_6^{3+}$ was used as an analog for magnesium hexahydrate (Cowan, 1993) to locate $Mg(H_2O)_6^{2+}$ binding sites (Kieft & Tinoco, 1997; Colmenarejo & Tinoco, 1999; Rüdisser & Tinoco, 2000) The RNA molecules used in this study are derived from the *Escherichia coli* RNase P RNA sequence and comprise nt 66–73 and 354–360 in the wild-type sequence; their sequences are shown in Figure 1. Two G•C base pairs were added at the 5′ end of the P4 stem to facilitate enzymatic synthesis, and the 3′ end was capped with a UUCG tetraloop and one additional A•U base pair to reduce the potential for formation of duplex structures.

RESULTS

Imino proton spectra

One-dimensional ^1H spectra acquired in H_2O at temperatures between 4 °C and 35 °C (15 °C spectrum shown in Fig. 2) show the imino proton resonances consistent with the secondary structures of the wild-type and mutant P4 molecules (Fig. 1). The G1 imino resonance of both molecules is not observed due to fast exchange with solvent. All imino proton resonances are assigned by standard procedures using data from H_2O NOESY and ^{15}N-^1H HSQC experiments (Varani & Tinoco, 1991; Varani et al., 1996). The unusually shifted imino resonance at 9.9 ppm in both the P4wt and P4m spectrum is characteristic of the UUCG tetraloop structure (Cheong et al., 1990; Allain & Varani, 1995), and confirms the formation of monomolecular stem-loop
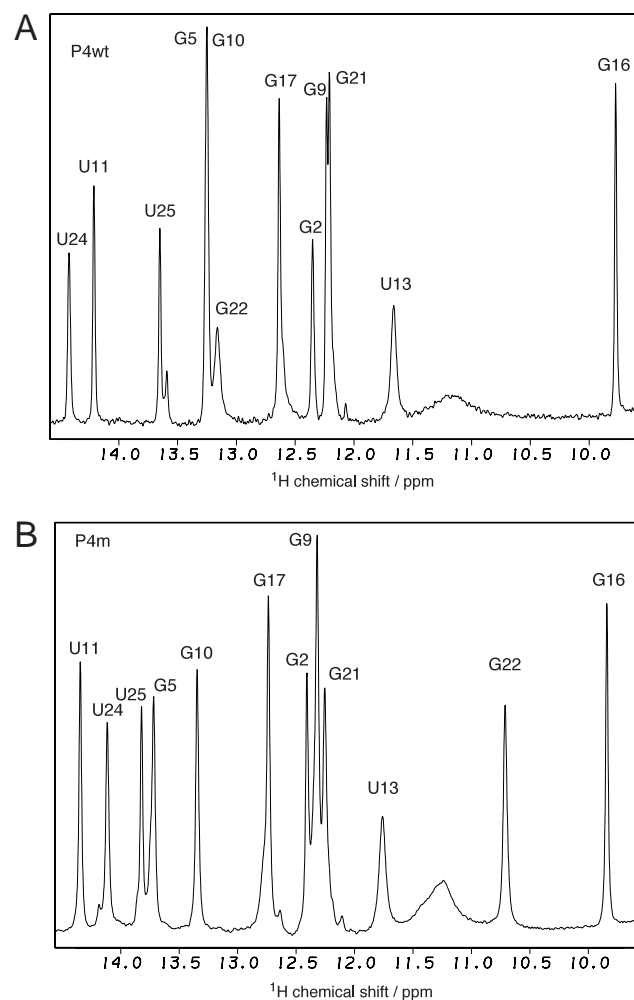

FIGURE 2. Imino proton spectra of P4wt (**A**) and P4m (**B**) at 15 °C. Spectra were acquired with 8,192 complex points and 512 scans on 0.4-mM RNA samples in 100 mM NaCl, 10 mM sodium phosphate, pH 6.4. The G1 imino resonance is not observed. All other imino proton resonances are labeled as assigned from H_2O NOESY experiments, and ^{15}N-^1H HSQC experiments.

structures for both molecules. The small imino proton resonance at 13.24 ppm in the P4wt spectrum indicates a faster exchanging imino proton; it was assigned to G22 based on cross-peaks to the G21 imino, G5 imino, and C7 amino protons and the ^{15}N chemical shift in ^{15}N-^1H HSQC experiments. The G22•C7 base pair is directly adjacent to the single uridine bulge and is apparently distorted or changed in solvent accessibility. The P4m spectra show an unusually shifted imino proton at 10.7 ppm, which was assigned to the guanine imino proton in the G22•U6 base pair based on the ^{15}N chemical shift in ^{15}N-^1H HSQC experiments (data not shown) and an NOE cross-peak between this resonance and the U6 imino proton. The U6 imino resonance at 12.35 ppm is weak and cannot be resolved from guanine imino resonances at 12.35 ppm in homonuclear experiments. It is unambiguously assigned from the ^{15}N chemical shift in ^{15}N-^1H HSQC experiments. The chemical shift for the G22 and U6 imino protons are consistent with formation of a G•U base pair. Only weak cross-peaks between the G22 and U6 imino protons are observed in the NOESY spectra, again indicating faster exchange with solvent for the U6 imino proton and a distortion of the base pairing geometry.

The most favorable spectral dispersion of resonances without loss of faster exchanging imino resonances was achieved at a temperature of 15 °C. This temperature was used in the majority of the NMR experiments. NOESY experiments at 15 °C and 150 ms mixing time in H_2O were used for assignment of exchangeable proton resonances. Sequential connectivity indicating close proximity of imino protons in stacked base pairs is observed from G2 through G5 and G22 through G16 in the P4wt molecule. The sequential cross-peak between G9 and G21 is not resolved due to the close proximity of the G9 and G21 chemical shifts. A weak cross-peak between G5 and G22 indicates continuation of base stacking across the bulge loop.

In the P4m spectra, sequential cross-peaks are observed from G2 through G22; an unusually weak G5–G22 cross-peak indicates distortion of the stacking geometry between G5 and G22. The G22–G21 cross-peak between the closing base pairs of the bulge loop is very weak. Stacking across the bulge loop appears to be significantly less pronounced in the P4m molecule.

Metal-ion binding constants from titrations

To analyze the binding affinity of the P4wt and P4m molecules for Mg^{2+}, $Co(NH_3)_6^{3+}$, and Ca^{2+}, imino proton chemical shift titrations were done with both P4wt and P4m molecules. Standard buffer conditions of
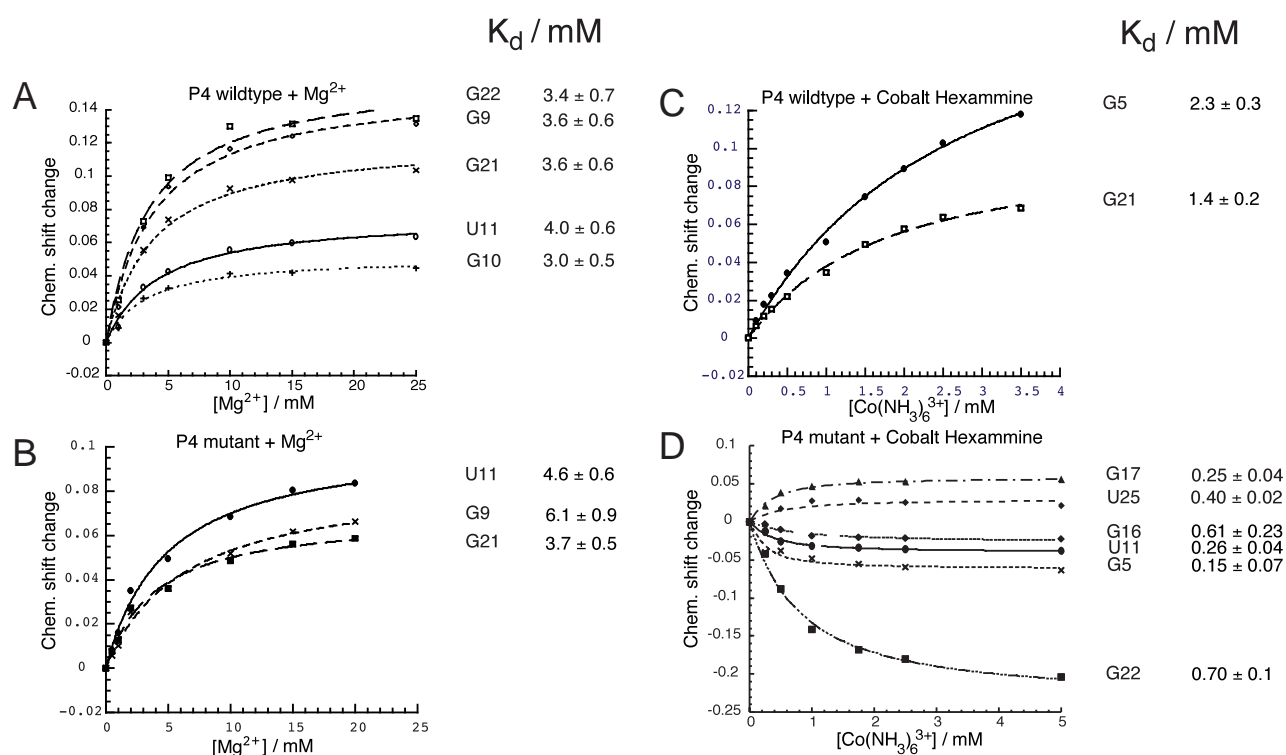
FIGURE 3. Imino proton chemical shift titration curves for Mg^{2+} and cobalt hexammine binding titrations recorded at 15 °C in 100 mM NaCl, 10 mM sodium phosphate, pH 6.4. Chemical shift changes for P4wt (**A**) and P4m (**B**) are plotted against the Mg^{2+} concentration. Titrations with cobalt hexammine are shown for P4wt (**C**) and P4m (**D**). On the right side of each panel, equilibrium binding dissociation constants (mM) determined from a fit of the data points to a single binding isotherm are given for those imino protons whose chemical shift could be accurately fitted.

100 mM NaCl, 10 mM sodium phosphate, pH 6.4, were used for Mg^{2+} and $Co(NH_3)_6^{3+}$ titrations. A buffer system of 100 mM NaCl, 5 mM d_{11}-Tris, pH 6.4, was used for Ca^{2+} titrations. Normalized titration curves are shown in Figures 3 and 4 for those imino protons showing a significant chemical shift change and binding affinity. The imino protons found to shift the most in the presence of Mg^{2+} are the G9, G10, U11, G21, and G22 imino protons in P4wt, and G9, U11, and G21 in P4m. Chemical shift changes for some of the other imino protons cannot be determined accurately because of peak overlap. Chemical shift changes were fit to a binding isotherm assuming a single binding site on the RNA as described by Gonzalez and Tinoco (1999). The resulting equilibrium dissociation constants are in the range of 2–5 mM as indicated in Figures 3 and 4.

Binding constants for Ca^{2+} binding to P4wt and P4m are 2.5 and 2.2 mM $\pm$ 0.5 mM and are nearly identical within the error margin. This is in good agreement with the essentially equal binding of Ca^{2+} to the wild-type

and mutant RNAs determined from kinetic experiments (Frank & Pace, 1997). A comparison of the binding constants superimposed on the secondary structure model (Fig. 5B) reveals that the site of Ca^{2+} binding appears to be very localized in the upper stem of P4wt at G9/G21, whereas P4m shows a significant contribution from G5 and U24 to Ca^{2+} binding. From the chemical shift titration data, a second binding site at U24 may be present.

The Mg^{2+} titration data show no significant difference in binding affinity between P4wt and P4m. The binding constants are 3.4 $\pm$ 0.5 mM for P4wt and 3.7 $\pm$ 0.5 mM for P4m. Superposition of the binding affinities on the secondary structure model in Figure 5A shows binding of Mg^{2+} localized close to the bulge loop in both molecules, with the largest changes determined
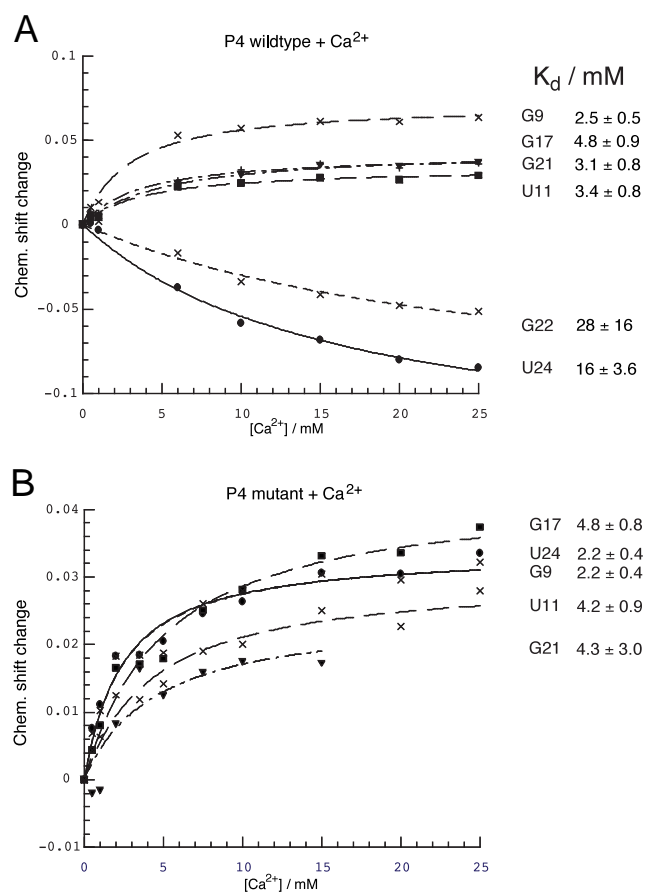

FIGURE 4. Imino proton chemical shift titration curves for Ca^{2+} titrations recorded at 15 °C in 100 mM NaCl, 5 mM d_{11}-Tris, pH 6.4. Chemical shift changes for P4wt (**A**) and P4m (**B**) are plotted against the Ca^{2+} concentration. On the right side, equilibrium binding dissociation constants (mM) determined from a fit of the data points to a single binding isotherm are given for those imino protons whose chemical shift could be accurately fitted.

FIGURE 5. Summary of the titration results in the context of the P4wt and P4m secondary structures. The relative magnitudes of binding affinities determined from specific imino protons are indicated by circles of different stroke weight. The location of the $Co(NH_3)_6^{3+}$ binding site as determined from intermolecular NOEs is indicated by the bullets next to the stems. **A**: Mg^{2+} titration results. **B**: Ca^{2+} titration results.

for G22 in P4wt and U11 in P4m. No significant chemical shift changes are seen for U24 in P4wt, and only a small change is seen in P4m. Both equilibrium constants are of the same order of magnitude as the Ca^{2+} equilibrium constants. The almost identical binding affinity between P4wt and P4m does not account for the difference in catalytic rates observed in kinetic studies and is in contrast to the reported Mg^{2+} concentration dependency of catalytic rates, from which a more than tenfold stronger binding to P4wt was concluded (Frank & Pace, 1997). Binding constants for both Mg^{2+} and Ca^{2+} are comparable with published data obtained on the hammerhead ribozyme (Menger et al., 1996).

The binding site populated by Mg^{2+} is somewhat removed from the J3/4 region implicated in binding of a catalytic Mg^{2+} ion from phosphorothioate interference studies and may not be directly involved in catalysis. The binding site close to U24 populated by Ca^{2+} in P4m appears close enough to the required phosphates at A3, A4, and G5 found by Kanzatsev and

Pace (1998) to explain participation of a Ca^{2+} ion bound at this site in catalysis.

Titration of P4wt with $Co(NH_3)_6^{3+}$ shows a similar pattern of chemical shift changes and binding constants for individual imino protons as the Mg^{2+} titration data (Fig. 3C). Binding of $Co(NH_3)_6^{3+}$ to P4wt is approximately 2.5-fold stronger than Mg^{2+} binding for the G21 imino proton. This difference is less than the 10- to 40-fold increase in binding of the cobalt ligand relative to Mg^{2+} that was observed in other RNA molecules (Kieft & Tinoco, 1997; Colmenarejo & Tinoco, 1999), which may indicate direct coordination of the magnesium ion to phosphate or carbonyl oxygen or to N7 nitrogen positions of purine bases. Similar titration experiments with P4m result in a tenfold stronger binding of the cobalt ligand compared to Mg^{2+}. The use of $Co(NH_3)_6^{3+}$ as an analog for Mg^{2+} for the purpose of localizing the Mg^{2+} binding site seems appropriate because of the similar location of the binding site as inferred from the similar pattern of chemical shift changes.

FIGURE 6. H_2O NOESY spectra of P4wt acquired at 150 ms, 15 °C in 6 mM $Co(NH_3)_6^{3+}$, 100 mM NaCl, 10 mM sodium phosphate, pH 6.4. The RNA concentration in this experiment was 2.2 mM. **A:** Imino–imino region (bottom) and imino–$Co(NH_3)_6^{3+}$ region (top) showing intermolecular cross-peaks between $Co(NH_3)_6^{3+}$ and RNA imino protons. The sequential connectivity between adjacent imino resonances is shown as a solid line. **B:** Aromatic-ribose region showing intermolecular cross-peaks between $Co(NH_3)_6^{3+}$ and aromatic and amino RNA protons. The inset on the left panel shows the localization of the intermolecular NOEs in the secondary structure. Strong cross-peaks are observed between $Co(NH_3)_6^{3+}$ and RNA protons of G5, G9, G10, and G21. Weaker cross-peaks to amino protons of C7, C8, C19, C20, and C23 and cross-peaks to aromatic protons of A4 and C20 are also observed.

Intermolecular Co(NH₃)₆³⁺–RNA NOE cross-peaks

The slowly exchanging $Co(NH_3)_6^{3+}$ ammine protons show a single resonance at 3.65 ppm in H_2O. Inter-molecular NOE cross-peaks between this $Co(NH_3)_6^{3+}$ ammine proton resonance and RNA imino, amino, and aromatic protons are observed in H_2O NOESY experiments in the presence of 6 mM $Co(NH_3)_6^{3+}$ at 150 ms mixing time (Figs. 6 and 7). All intermolecular NOE cross-peaks have positive sign compared to the diagonal peaks, but vary in intensity and line width. The cross-peak line width generally reflects the RNA proton line width. The intermolecular cross-peaks to RNA imino protons are unambiguously assigned with the exception of the overlapped G9 and G21 imino cross-peaks in the P4m spectra. The presence of intermolecular NOEs to both the G21 H8 and the C20 H6 and amino protons was used to confirm the existence of NOEs to both G9 and G21 imino protons in the P4m RNA.

NOE cross-peak intensities for imino and aromatic protons are summarized in the inset secondary structures of P4wt and P4m in Figures 6 and 7. The $Co(NH_3)_6^{3+}$ appears to be localized at the bottom of the upper stem directly adjacent to the bulge loop in both molecules. Distance constraints derived from these cross-peaks are used in structure calculations to locate the site of $Co(NH_3)_6^{3+}$ binding in the RNA structure. From H_2O NOESY data, no significant changes in the intensities or connectivities of RNA–RNA cross-peaks could be observed with $Co(NH_3)_6^{3+}$, suggesting little or no structural changes upon $Co(NH_3)_6^{3+}$ binding.

Assignments of nonexchangeable protons and structure calculations

As evident from the aromatic-H1′ proton NOE spectra shown in Figure 8, the wild-type molecule displays sequential connectivities as expected from the proposed secondary structure. The sequential connectivities ex-
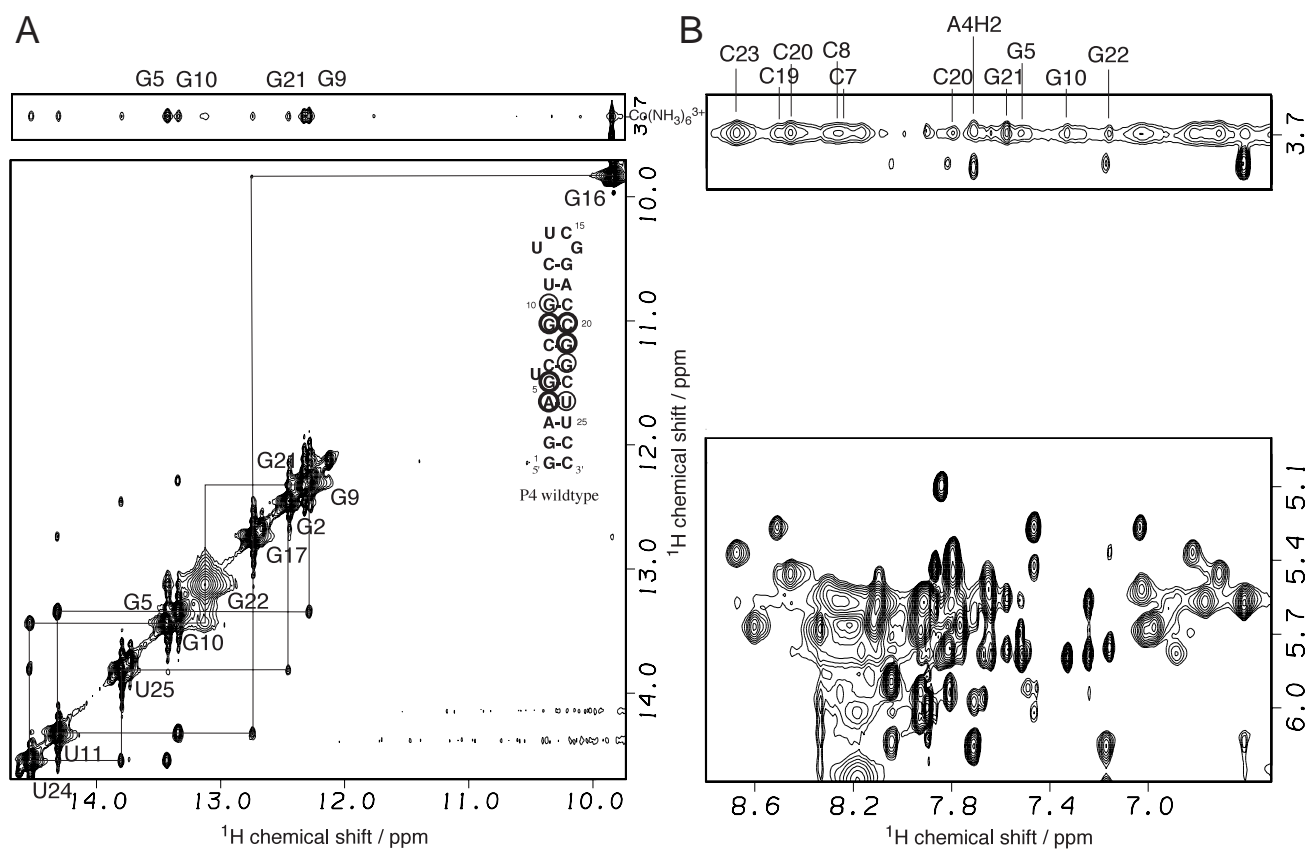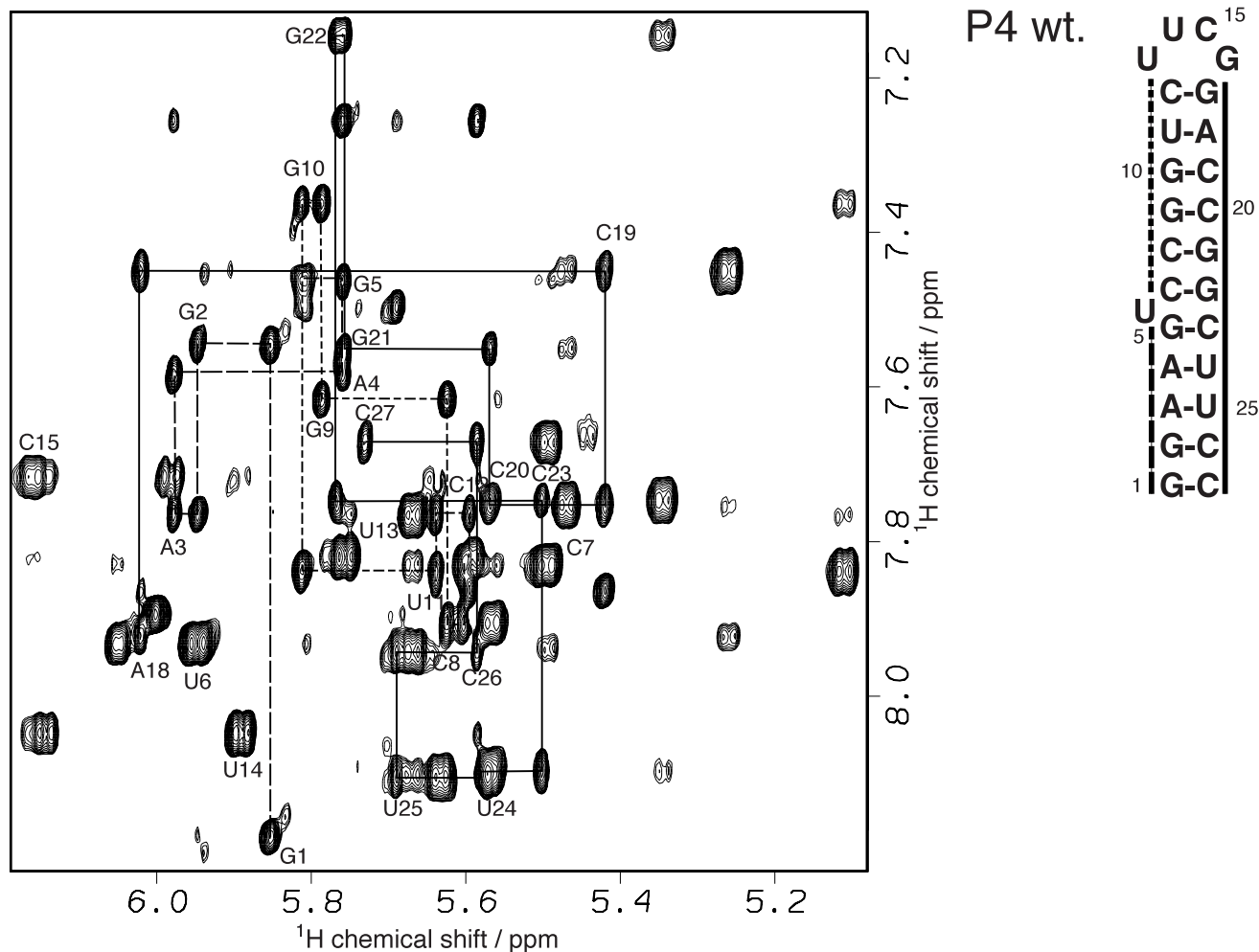

FIGURE 7. H_2O NOESY spectra of P4m acquired at 150 ms, 15 °C in 6 mM $Co(NH_3)_6^{3+}$, 100 mM NaCl, 10 mM sodium phosphate, pH 6.4. The RNA concentration in this experiment was 2.2 mM. **A:** Imino–imino region (bottom) and imino–$Co(NH_3)_6^{3+}$ region (top) showing intermolecular cross-peaks between $Co(NH_3)_6^{3+}$ and RNA imino protons. The sequential connectivity between adjacent imino resonances is shown as a solid line in the bottom panel. **B:** Aromatic-ribose region showing intermolecular cross-peaks between $Co(NH_3)_6^{3+}$ and aromatic and amino RNA protons. The inset on the left panel shows the localization of the intermolecular NOEs at the secondary structure level. Strong cross-peaks are observed between $Co(NH_3)_6^{3+}$ and RNA protons of G5, G9, G10, and G21. Weaker cross-peaks to amino protons of C20 and C23 and cross-peaks to aromatic protons of G5, C20, G21, and 23 are also observed.

FIGURE 8. Aromatic-H1′ region of a 400-ms D_2O NOESY spectrum of P4wt at 15 °C in 100 mM NaCl, 10 mM sodium phosphate, pH 6.4. Strong sequential H1′-aromatic connectivities indicative of regular A-form helical geometry are indicated by lines. Long dashed line: G1–G5, short dashed line: C7–U13, solid line: G17–C27. The sequential walk is interrupted between G5 and C7, indicating a nonstacking position of U6. Weak sequential cross peaks between G5 and C7 suggest weaker stacking between these residues. Sequential connectivity is continuous between G17 and C27, indicating regular stacking geometry along the whole strand.

tend from G1 to G5 and from C7 to U13 on the bulged strand, with weaker A-form-like sequential cross-peaks observed across the bulge loop between G5 and C7, suggestive of stacking interaction between these two bases. These data require the bulge nucleotide to be in a nonstacked, extrahelical conformation. A-form connectivity is observed on the opposite strand through the bulge loop from G17 to C27, lending further support for stacking between the two stems. No indication of conformational dynamics of the G22•C7 base pair was found in NOESY or ^1H-^1H COSY spectra.

For the mutant P4m molecule (Fig. 9), A-form sequential connectivity is observed from G1 to U6 and from C8 to U13 on the bulged strand. Again, A-form sequential cross-peaks are observed between U6 and C8, somewhat weaker than the G5–C7 connectivities observed in P4wt. This indicates that the U7 intro-

duced by mutation is bulged out instead of the U6 in the wild-type molecule. The assignment of U6 as the base-paired nucleotide is based on sequential connectivity between G5 and U6, which is corroborated by observation of a strong $^3J_{PH3'}$ and missing $^3J_{PH5'}$ coupling at the U6 phosphorus, indicating A-form stacking between G5 and U6. Conversely, the lack of a strong sequential cross-peak between either uridine residue to C8 does not support a stacked conformation for U7. On the opposite strand, A-form connectivity is again present from G17 to C27, indicating a stacked conformation of the base pairs closing the bulge loop.

The UUCG tetraloop in both molecules displays the characteristic spectral properties described earlier (Cheong et al., 1990; Allain & Varani, 1995). Unusually shifted H1′ of G17 and H3′ of G16 and *syn* conformation of G16 were confirmed easily.
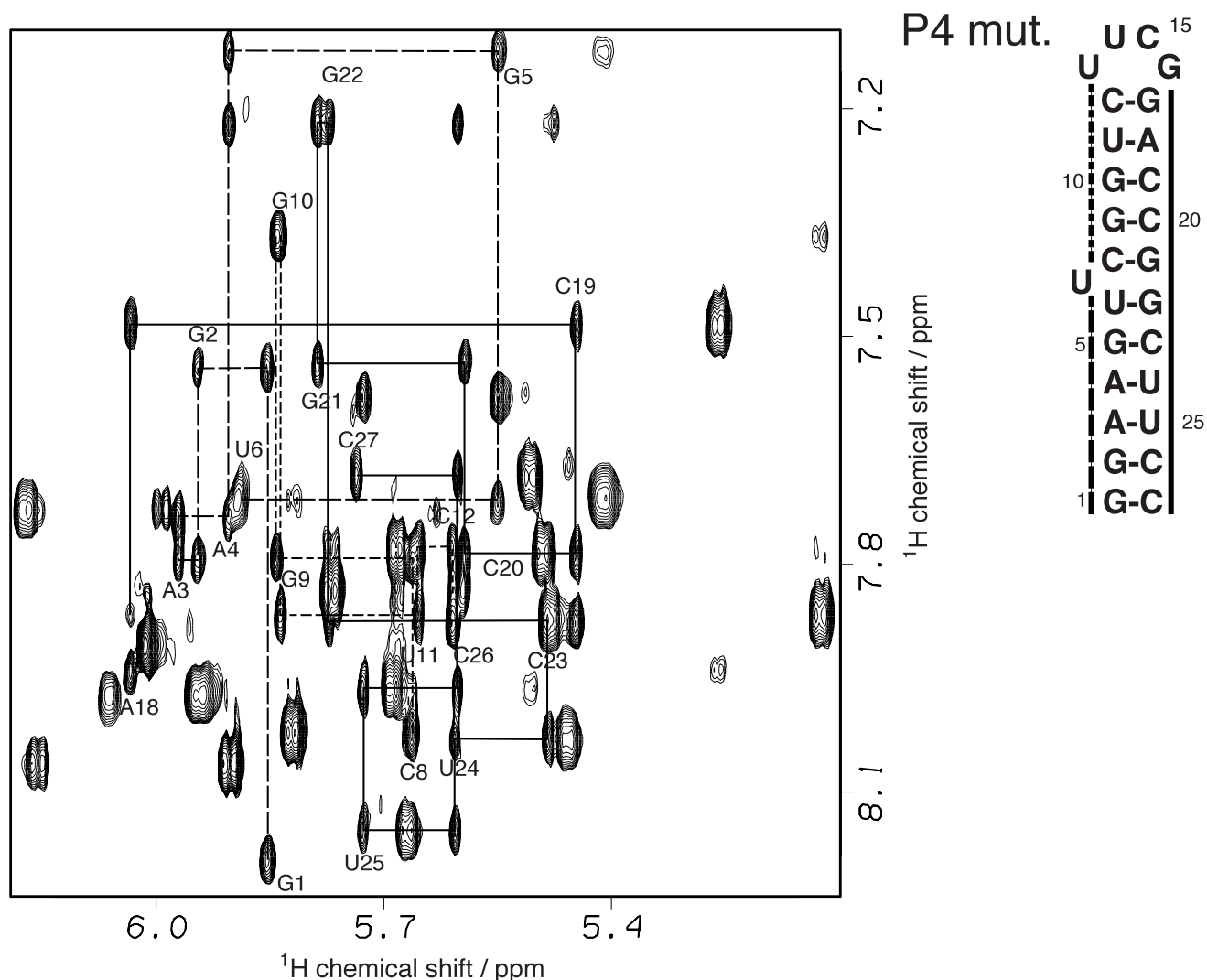
FIGURE 9. Aromatic-H1′ region of a 400-ms D_2O NOESY spectrum of P4m at 15 °C in 100 mM NaCl, 10 mM sodium phosphate, pH 6.4. Strong sequential H1′-aromatic connectivities indicative of regular A-form helical geometry are indicated by lines. Long dashed line: G1–U6, short dashed line: C8–U13, solid line: G17–C27. The sequential walk is interrupted between U6 and C8, indicating a nonstacking position of U7. Weak sequential cross peaks between U6 and C8 suggest weak stacking between those residues. Sequential connectivity is continuous between G17 and C27, indicating regular stacking geometry along the whole strand.

The sequential connectivity patterns demonstrated for the aromatic-H1′ spectral regions could be confirmed in the H1′–ribose, ribose–aromatic, and aromatic–aromatic regions. Based on the sequential assignments of H1′ and aromatic protons, all H2′ protons and all but a few H3′ and H4′ protons could be unambiguously assigned from ^1H-^1H COSY, NOESY, and ^{13}C-^1H HMQC experiments.

The conformation of the bulged nucleotide is determined by a number of unusual NOEs in both molecules. A weak H1′–H3′ NOE between G5 and U6 in P4wt combined with weaker H1′–H6 and H2′–H5 cross-peaks determine the P4wt bulge conformation. The intense H2′–H6 cross-peak typical for A-form conformation is completely absent. The only cross-peak

observed between U6 and C7 is a weaker than usual H3′–H6 cross-peak. The P4m bulge conformation is determined by the absence of all U6 ribose to U7 aromatic and ribose cross-peaks except for a weak H2′–H6 cross-peak. Cross-peaks between U7 and C8 are weaker than usual except for a weak H4′–H6 cross-peak not usually observed in A-form RNA.

NOESY cross-peak intensities were estimated from a set of NOESY experiments at various mixing times, and distance constraints were obtained from classification of the cross-peak intensities into four distance categories as described in detail in Materials and Methods. NOESY experiments in the presence of Mg^{2+}, $Co(NH_3)_6^{3+}$, or Ca^{2+} did not show significant changes in cross-peak intensities or connectivities compared

to experiments in the absence of divalent metal ions. The same set of distance constraints was therefore used in structure calculations for both free RNA and the RNA–Co(NH$_3$)$_6^{3+}$ complex. Dihedral constraints for ribose and backbone conformation were derived from high resolution, phosphorus-decoupled ^{1}H-^{1}H COSY experiments and ^{31}P-^{1}H correlation experiments as described in Materials and Methods. Based on the magnitude of $^3J_{H1'H2'}$, sugar pucker was constrained to 3′-endo for all nucleotides except G5 and U6, which were constrained to range between 2′-endo and 3′-endo, and U14 and C15, which were constrained to be 2′-endo in P4wt. For P4m, U6 was constrained to range between 2′-endo and 3′-endo and U7, U14, and C15 were constrained as 2′-endo; all other nucleotides were constrained 3′-endo. O4′-exo conformation for G5 and U6 could be excluded based on the intraresidue H1′–H4′ NOE intensity. Backbone dihedral angles that could not be directly measured were constrained to A-form ranges in the helical regions only. Conformation angles ϵ were found to be within A-form range on the nonbulged strand based on measurement of $^3J_{PH3'}$. The α conformation angle of U7 and ζ conformation angle of U6 in the P4m molecule were constrained to be non-*trans* because of the unusual chemical shift of the U7 phosphorus resonance.

Table 1 summarizes the statistics on distance and dihedral constraints used in the structure calculations for the P4wt and P4m molecules. Of the 50 initial structures, 35 structures converged during the global fold stage as judged from NOE violation energies. During subsequent refinement, 11 (P4wt) and 21 (P4m) structures converged to low NOE and dihedral angle violation energies. The converged structures of both P4wt

and P4m were analyzed and most of the structures were found to fall in a single structure family. Structures that differed from the major structure family for each RNA revealed proton–proton distances below 5 Å for which no NOE cross-peaks were observed even at long mixing time; three structures for P4wt and four structures for P4m were discarded from further analysis based on this criterion. Converged structures from the refinement stage were superimposed using X-PLOR (Brünger, 1993) for calculation of RMS deviations and average structures. The average structure was energy minimized to resolve distortion of base geometries introduced by the averaging. All-atom average RMSD values of individual structures to the average structure are given in Table 1.

Both the P4wt and P4m structures show a marked bend at the site of the bulge loop. The bulged nucleotide is found in the minor groove for P4wt, whereas it is oriented towards the major groove in the P4m structure (Fig. 10). The bending of the two structures is roughly consistent with preliminary results from ^{15}N-^{1}H residual dipolar couplings (data not shown).

Structure calculations on the RNA–Co(NH$_3$)$_6^{3+}$ complex were done to locate the site of Co(NH$_3$)$_6^{3+}$ binding. After refinement, 11 structures for the P4wt–Co(NH$_3$)$_6^{3+}$ complex and 12 structures for the P4m–Co(NH$_3$)$_6^{3+}$ complex were selected for averaging. The average structures are shown in Figure 10. The Co(NH$_3$)$_6^{3+}$ is located in the major groove at the bottom of the upper stem in the P4wt–Co(NH$_3$)$_6^{3+}$ complex structure. It is in close proximity to the G5–C23, C8–G21, and G9–C20 base pairs. In the P4m–Co(NH$_3$)$_6^{3+}$ complex structure, the Co(NH$_3$)$_6^{3+}$ is located at the top of the upper stem, close to the G5–C23, U6–G22, and C8–G21 base pairs. The overall structural features of the RNA appear unchanged

TABLE 1. Structure constraints and statistics.

| Molecule	P4wt	P4m	P4wt complex	P4m complex
NOE constraints				
Intraresidue	69	65	69	65
Interresidue	197	203	197	203
Base pairing	48	49	48	49
Intermolecular	n.a.[a]	n.a.	12	12
Total	314	317	326	329
Number per nucleotide	9.9	9.9	10.3	10.4
Torsion constraints				
Global fold	153	152	153	152
Refinement	245	246	245	246
Structural statistics of individual structures				
NOE violations > 0.2 Å	1	1	1	1
Dihedral violations > 5°	1	2	1	2
Structural statistics of average structure				
NOE violations > 0.2 Å	0	0	1	0
Dihedral violations > 5°	1	1	1	1
RMS deviation to average	1.84	1.94	1.66	1.46

[a] n.a.: not applicable.
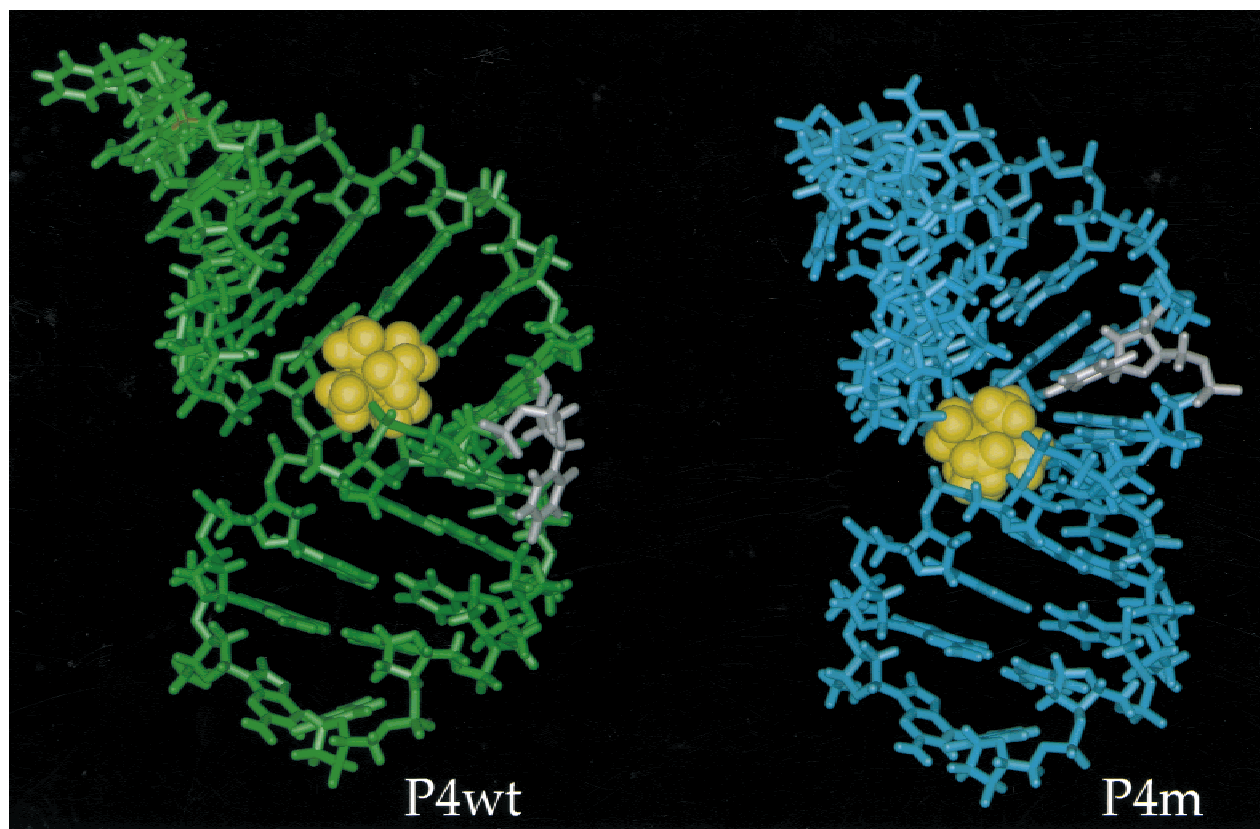
FIGURE 10. Side view of the average structures for the P4wt (left) and P4m (right) RNA–Co(NH$_3$)$_6^{3+}$ complexes. The bulged uridine nt 6 (P4wt) and 7 (P4m) are colored white; all other nucleotides are colored green (P4wt) and cyan (P4m). The Co(NH$_3$)$_6^{3+}$ molecule is shown as spheres. The bulged uridine occupies a position in the minor groove of the lower stem for P4wt, whereas it is located in the major groove of the upper stem for P4m. The bound Co(NH$_3$)$_6^{3+}$ is located at the site of the bend slightly above the bulge loop in P4wt, and appears close to the G5:C23 and U6:G22 base pairs slightly below the bulge loop in P4m. Comparing P4wt and P4m, the position of the bound Co(NH$_3$)$_6^{3+}$ shifts down to the lower stem by more than 1 bp.

except for a more pronounced bend of the P4wt structure, which is likely caused by the additional intermolecular constraints to Co(NH$_3$)$_6^{3+}$.

DISCUSSION

Comparison of the structures of wild-type and mutant P4 stems reveals a significant difference between the two molecules. Upon mutation of C70 to U, a G•U base pair is introduced involving U69, thus extending the 5′ half of the P4 stem and shifting the bulge position by 1 nt towards U70. This difference in secondary structure between P4wt and P4m is evident from the sequential NOESY cross-peaks shown in Figures 8 and 9. In addition to this change in bulge position, structure calculations based on NOE distance restraints and torsion angle restraints show that the bulged uridine changes from a minor grove position to the major groove. Both the change in bulge position and the introduction of a G•U pair with the expected widening of the major groove explain the change in positioning of the bound metal ion as illustrated in Figure 5.

The change in the bulge nucleotide position in the mutant additionally contributes to displacing the metal ion from the position occupied in the wild-type structure by steric exclusion. Such a change in position of the bound metal ion might, in the case of Ca^{2+}, effect improved efficiency of the metal ion for catalysis while preserving the magnitude of the binding constant. In the case of Mg^{2+} and Co(NH$_3$)$_6^{3+}$, a metal ion binding closer to the 5′ terminus of the P4 element in the mutant might interfere with binding of the catalytic Mg^{2+} ion further 5′ in the P4 stem and the J2/4 junction.

Comparison of the metal-ion binding properties of the P4wt and P4m molecules shows only a moderate difference between Mg^{2+} and Ca^{2+}. Differences in equilibrium binding constants between P4wt and P4m are within the margin of error for both metals. The very similar Ca^{2+} binding properties of P4wt and P4m are consistent with binding constants determined on the full-length RNase P RNA (Frank & Pace, 1997). The similar binding constants determined for Mg^{2+} binding by both molecules do not agree with findings on the full-length RNase P RNA, where a more than tenfold

decrease in magnesium binding affinity was observed for the mutant. Neither the large difference in catalytic rates in the presence of Mg^{2+} and Ca^{2+} for wild-type and mutant nor the fourfold increase in catalytic rate in Ca^{2+} for the mutant RNase P can be explained by the binding constants measured from the isolated P4 elements. This discrepancy is most likely due to contributions of the flanking J3/4 and J2/4 single-stranded regions in binding the catalytic Mg^{2+} ion in the full RNase P structure that is missing in the isolated P4 element.

We expect that the change in secondary structure and bulge nucleotide position we found for the mutant P4 does occur in the context of the full RNase P RNA. However, the Mg^{2+} binding site determined by this study may not correspond to the site of catalytic Mg^{2+} binding.

A potential structural role for a divalent metal ion bound at the site of the bulge loop arises with a putative tertiary interaction between L8 and the minor groove of P4 at the G•C base pairs 3′ to the bulge loop as proposed by Massire et al. (1998). In the context of the compact RNase P tertiary structure as reported by the Pace and Westhof groups (Harris et al., 1994; Massire et al., 1998), such a local change to the P4 structure would be expected to propagate to other parts of the structure at the active site. The proposed L8–P4 interaction provides a possible mechanism for structural distortion beyond P4. In particular, the change in position of the universally conserved bulged uridine could have a profound effect if functional groups on the bulged nucleotide participate in tertiary contacts. This is an example of how a single base mutation can change the global conformation of an RNA.

MATERIALS AND METHODS

RNA synthesis

Wild-type and mutant P4 RNAs were enzymatically synthesized from a synthetic DNA template using T7 RNA polymerase (Milligan et al., 1987; Wyatt et al., 1991). The RNA product was precipitated with ethanol and purified on 20% denaturing polyacrylamide gels. The 27-nt full-length product was isolated from the gel by electroelution. The eluant was precipitated with ethanol and dialyzed against the buffer used for NMR experiments. Typical sample concentrations as measured by UV absorbance were 2.2–2.4 mM. Samples for nonexchangeable proton spectra were repeatedly lyophilized and resuspended in 99.96% D_2O to remove residual H_2O solvent.

Uniformly ^{15}N-labeled RNA was transcribed from labeled NTPs obtained from RNA purified from *E. coli* grown on minimal media with ^{15}N NH_4Cl as sole nitrogen source. Uniformly $^{13}C/^{15}N$-labeled RNA was transcribed from NTPs prepared from RNA obtained from *Methylophilus methylotrophus* grown on minimal media with ^{13}C methanol and ^{15}N $(NH_4)_2SO_4$ as sole carbon and nitrogen sources. Isotope-labeled RNA harvested from these cells was digested to mononucleotides using RNase P1. After purification on a boronate affinity column (AffiGel 601, BioRad), nucleotide monophosphates were enzymatically phosphorylated to triphosphates (Batey et al., 1992, 1995; Nikonowicz et al., 1992).

NMR spectroscopy

All NMR experiments were done on Bruker AMX 600 and DRX 500 spectrometers at temperatures of 15 and 30 °C. Exchangeable proton spectra were acquired in 90% H_2O/10% D_2O, 100 mM NaCl, 10 mM Na-phosphate, pH 6.4. Non-exchangeable proton spectra were acquired in 99.96% D_2O, 100 mM NaCl, 10 mM Na-phosphate, pH 6.4. Proton chemical shifts were internally referenced to the solvent resonance. Unless otherwise noted in the text, sample volumes of 250 μL in Shigemi microcells were used for the experiments.

Exchangeable one-dimensional proton spectra in 90% H_2O/10% D_2O were acquired using jump-return solvent suppression. The excitation maximum was set to 11 ppm. Sample concentrations of 0.3–0.8 mM RNA in 500 μL volume were used for one-dimensional chemical shift titration experiments.

NOESY experiments in 90% H_2O/10% D_2O were performed at NOE mixing times of 150 and 300 ms and temperatures of 5, 10, 15, and 25 °C using jump-return water suppression (Sklenár & Bax, 1987) and z-gradient pulses during the NOE mixing time. NOESY experiments in D_2O (Macura et al., 1982) were performed at NOE mixing times of 50, 100, 150, 200, 300, and 400 ms. A presaturation pulse on the HDO resonance was used for solvent suppression. Zero and double quantum artifacts in the short mixing time experiments were suppressed by a z-gradient pulse during the mixing time and by incrementing the mixing time by 10 μs between t1 increments. NOESY spectra in D_2O were primarily acquired at 15 °C. Individual experiments were performed at 20, 25, and 30 °C. Four hundred to 512 FIDs of 2,048 complex points and 24 or 32 scans were acquired on the DRX 500 spectrometer.

Double quantum-filtered COSY experiments (Shaka & Freeman, 1983; Müller et al., 1986) were performed at 15 and 30 °C on the AMX 600 spectrometer. Broad-band decoupling of phosphorus using GARP1 (Shaka et al., 1985) was used in high-resolution COSY experiments.

Proton-detected ^{31}P-^{1}H COSY experiments were acquired at 600.14 MHz with 1,600 Hz spectral width in the ^{31}P dimension and 2,000 Hz spectral width in the ^{1}H dimension. Forty-eight scans of 2,048 complex points and 320 FIDs were acquired. A ^{31}P-^{1}H hetero-TOCSY-NOESY experiment (Kellogg, 1992; Kellogg et al., 1992; Kellogg & Schweitzer, 1993) was performed at 15 °C using a 70-ms DIPSI2 mixing pulse (Rucker & Shaka, 1989) and 500-ms NOESY mixing time. Ninety-six FIDs of 2,048 complex points from 240 scans were acquired.

We ran ^{15}N-^{1}H FHSQC experiments (Mori et al., 1995) on uniformly labeled ^{15}N samples in 90% H_2O/10% D_2O using the 3-9-19 WATERGATE for solvent suppression (Sklenár et al., 1993) with a sweep width of 2,500 Hz in the ^{15}N dimension and the ^{15}N carrier at 150 ppm. We acquired 256 FIDs of 2,048 complex points with 8 scans.

NOE distance constraints

NOE cross-peak intensities at 50, 100, and 150 ms mixing time were estimated from NOESY experiments acquired at 15 °C

in D_2O. Cross-peaks were classified as strong (1.8–3.2 Å), medium (2.0–4.0 Å), weak (2.5–5.0 Å), and very weak (3.0–7.0 Å). All cross-peaks only visible at 400 ms mixing time were classified as very weak. No distance constraints were derived from NOESY experiments in H_2O except for intermolecular cross-peaks between RNA and $Co(NH_3)_6^{3+}$ and base pairing constraints. These intermolecular cross-peaks were classified as strong (4.3–5.0 Å) and medium (4.3–7.0 Å), accounting for the distance of 2.5 Å between the central Co atom and the amine protons. Distance ranges different from those for nonexchangeable protons are used because nonuniform excitation and exchange with solvent complicate quantitation of NOE cross-peak intensities from exchangeable protons.

Hydrogen-bonding constraints were used to define base-pairing geometry for all base pairs for which imino protons were observed in the 150-ms H_2O NOESY experiments. Hydrogen-bonding constraints for the C7:G22 base pair were slightly relaxed because of the larger imino proton line width. The non-Watson–Crick U13:G16 in the tetraloop was constrained based on the published tetraloop structure (Cheong et al., 1990); constraints for this base pair were relaxed similar to the C7:G22 base pair.

Dihedral constraints

Sugar conformation was constrained to 3′-endo, 2′-endo, or a range of conformations from 3′-endo to 2′-endo based on the observed H1′–H2′ coupling constants. The sugar conformation angles ν_1 to ν_4 were used to constrain the sugar pucker instead of δ. The glycosidic conformation angle χ was constrained to *anti* for all nucleotides except G16, based on the strong H8–H1′ NOE cross-peak observed for this nucleotide. The backbone conformation angle β was constrained as *trans* for nucleotides without observable $^3J_{PH5'}$ or $^3J_{PH5''}$ and constrained as non-*trans* if either $^3J_{PH5'}$ or $^3J_{PH5''}$ were large enough to result in sufficiently intense cross-peaks. The backbone conformation angle γ was constrained to gauche$^+$ in both stem regions based on the absence of strong H4′–H5′ or H4′–H5″ cross-peaks in the DQF-COSY spectra. The backbone conformation angle ϵ was constrained based on estimated $^3J_{PH3'}$ couplings from DQF-COSY and ^{31}P-^1H COSY spectra. Lower limits of 5 Hz for $^3J_{PH3'}$ constrain ϵ to *trans* for 3′-endo sugar conformation (Varani et al., 1996). The α and ζ conformation angles were constrained to gauche minus for nucleotides with phosphorus chemical shift between -4 and -5 ppm. No constraints on α and ζ were used otherwise.

Structure calculations

Structures were calculated using X-PLOR 3.1 (Brünger, 1993) for restrained molecular dynamics. Initial structures were generated using random torsion angles. The molecular dynamics protocol was as described previously (Wimberly, 1992) and consists of two stages. Fifty randomized starting structures were subjected to the global fold stage of the protocol that utilizes NOE restraints and dihedral restraints for sugar pucker and glycosidic conformation angle. Structures with low NOE violation and total energy were selected for the subsequent refinement stage utilizing the full set of NOE and dihedral restraints. Structures with low NOE violation energies after

refinement were analyzed, and average structures were calculated from the final set of converged structures.

Complex structures were calculated by merging the RNA random torsion angle starting structures and $Co(NH_3)_6^{3+}$ before the first stage. The same sets of intramolecular NOE and torsion angle constraints were used for the complex structures, as the NOE spectra did not differ significantly.

The coordinates for several structures of each molecule have been deposited in the PDB data file; the ID codes are: P4wt (1F7F), P4m (1F7G), P4wt-hexammine complex (1F7H), P4m-hexammine complex (1F7I).

REFERENCES

Allain FHT, Varani G. 1995. Divalent metal ion binding to a conserved wobble pair defining the upstream site of cleavage of group I self-splicing introns. *Nucleic Acids Res 23*:341–350.

Batey RT, Battiste JL, Williamson JR. 1995. Preparation of isotopically enriched RNAs for heteronuclear NMR. *Methods Enzymol 261*:300–322.

Batey RT, Inada M, Kujawinski E, Puglisi JD, Williamson JD. 1992. Preparation of isotopically labeled ribonucleotides for multidimensional NMR spectroscopy of RNA. *Nucleic Acids Res 20*:4515–4523.

Brünger AT. 1993. *X-PLOR Version 3.1: A system for X-ray crystallography and NMR*. New Haven, Connecticut: Yale University Press.

Chen JL, Nolan JM, Harris ME, Pace NR. 1998. Comparative photocross-linking analysis of the tertiary structures of *Escherichia coli* and *Bacillus subtilis* RNase P RNAs. *EMBO J 17*: 1515–1525.

Cheong C, Varani G, Tinoco I Jr. 1990. Solution structure of an unusually stable RNA hairpin, 5′GGAC(UUCG)GUCC. *Nature 346*:680–682.

Colmenarejo G, Tinoco I Jr. 1999. Structure and thermodynamics of metal binding in the P5 helix of a group I intron ribozyme. *J Mol Biol 290*:119–135.

Cowan JA. 1993. Metallobiochemistry of RNA. $Co(NH_3)_6^{3+}$ as a probe for Mg^{2+}(aq) binding sites. *J Inorg Biochem 49*:171–175.

Frank DN, Ellington AD, Pace NR. 1996. In vitro selection of RNase P RNA reveals optimized catalytic activity in highly conserved structural domain. *RNA 2*:1179–1188.

Frank DN, Pace NR. 1997. In vitro selection for altered divalent metal specificity in the RNase P RNA. *Proc Natl Acad Sci USA 94*:14355–14360.

Gonzalez RL Jr, Tinoco I Jr. 1999. Solution structure and thermodynamics of a divalent metal ion binding site in an RNA pseudoknot. *J Mol Biol 289*:1267–1282.

Guerrier-Takada C, Gardiner K, Marsh T, Pace N, Altman S. 1983. The RNA moiety of ribonuclease P is the catalytic subunit of the enzyme. *Cell 35*:849–857.

Guerrier-Takada C, Haydock K, Allen L, Altman S. 1986. Metal ion requirements and other aspects of the reaction catalyzed by M1 RNA, the RNA subunit of ribonuclease P from *Escherichia coli*. *Biochemistry 25*:1509–1515.

Hardt W-D, Erdmann VA, Hartmann RK. 1996. Rp-deoxy-phosphorothioate modification interference experiments identify 2′-OH groups in RNase P RNA that are crucial to tRNA binding. *RNA 2*:1189–1198.

Harris ME, Frank DN, Pace NR. 1998. Structure and catalytic function of the bacterial ribonuclease P enzyme. In: Simons, RW, Grunberg-Manago M, eds. *RNA structure and function.* Cold Spring Harbor, New York: Cold Spring Harbor Laboratory Press. pp 309–337.

Harris ME, Nolan JM, Malhotra A, Brown JW, Harvey S, Pace NR. 1994. Use of photoaffinity crosslinking and molecular modeling to analyze the global architecture of ribonuclease P RNA. *EMBO J 13*:3953–3963.

Harris ME, Pace NR. 1995. Identification of phosphates involved in catalysis by the ribozyme RNase P RNA. *RNA 1*:210–218.

Kanzatsev AV, Pace NR. 1998. Identification by modification-interference of purine N-7 and ribose 2′-OH groups critical for catalysis by bacterial ribonuclease P. *RNA 4*:937–947.

Kellogg GW. 1992. Proton-detected hetero-TOCSY experiments with application to nucleic acids. *J Magn Reson 98*:176–182.

Kellogg GW, Schweitzer BI. 1993. Two- and three-dimensional ^{31}P-driven NMR procedures for complete assignment of backbone resonances in oligodeoxyribonucleotides. *J Biomol NMR 3*:577–595.

Kellogg GW, Szewczak AA, Moore PB. 1992. Two-dimensional hetero-TOCSY-NOESY. Correlation of ^{31}P resonances with anomeric and aromatic 1H Resonances in RNA. *J Am Chem Soc 114*:2727–2728.

Kieft JS, Tinoco I Jr. 1997. Solution structure of a metal binding site in the major groove of RNA complexed with cobalt (III) hexammine. *Structure 5*:713–721.

Macura S, Wüthrich K, Ernst RR. 1982. Separation and suppression of coherent transfer effects in two-dimensional NOE and chemical exchange spectroscopy. *J Magn Reson 46*:269–282.

Massire C, Jaeger L, Westhof E. 1998. Derivation of the three-dimensional architecture of bacterial ribonuclease P RNA from comparative sequence analysis. *J Mol Biol 279*:773–793.

Menger M, Tuschl T, Eckstein F, Pörschke D. 1996. Mg^{2+}-dependent conformational changes in the hammerhead ribozyme. *Biochemistry 35*:14710–14716.

Milligan JF, Groebe DR, Witherell GW, Uhlenbeck OC. 1987. Oligoribonucleotide synthesis using T7 RNA polymerase and synthetic DNA templates. *Nucleic Acid Res 15*:8783–8798.

Mori S, Abeygunawardana C, Johnson MO, van Zijl PCM. 1995. Improved sensitivity of HSQC spectra of exchanging protons at short interscan delays using a new fast HSQC (FHSQC) detection scheme that avoids water saturation. *J Magn Reson, Series B 108*:94–98.

Müller N, Ernst RR, Wüthrich K. 1986. Multiple-quantum-filtered two-dimensional correlated NMR spectroscopy of proteins. *J Am Chem Soc 108*:6482–6492.

Nikonowicz EP, Sirr A, Legault P, Jucker FM, Baer LM, Pardi A. 1992. Preparation of ^{13}C and ^{15}N labelled RNA for heteronuclear multi-dimensional NMR studies. *Nucleic Acids Res 20*:4507–4513.

Pace NR, Brown JW. 1995. Evolutionary perspective on the structure and function of ribonuclease P, a ribozyme. *J Bacteriol 177*:1919–1928.

Rucker SP, Shaka AJ. 1989. Broadband homonuclear cross polarization in 2D N.M.R. using DIPSI-2. *Mol Phys 68*:509–517.

Rüdisser S, Tinoco I Jr. 2000. Structure and thermodynamics of metal-ion binding to G•A mismatches and to the GAAA tetraloop. *J Mol Biol 295*:1211–1223.

Shaka AJ, Barker PB, Freeman R. 1985. Computer-optimized decoupling scheme for wideband applications and low-level operation. *J Magn Reson 64*:547–522.

Shaka AJ, Freeman R. 1983. Simplification of NMR spectra by filtration through multiple-quantum coherence. *J Magn Reson 51*:169–173.

Sklenár V, Bax A. 1987. Spin-echo water suppression for the generation of pure-phase two-dimensional NMR spectra. *J Magn Reson 74*:469–479.

Sklenár V, Piotto M, Leppik R, Saudek V. 1993. Gradient-tailored water suppression for ^{1}H-^{15}N HSQC experiments optimized to retain full sensitivity. *J Magn Reson, Series A 102*:241–245.

Varani G, Aboul-ela F, Allain FH-T. 1996. NMR investigation of RNA structure. *Prog Nucl Mag Reson Spectrosc 29*:51–127.

Varani G, Tinoco I Jr. 1991. RNA structure and NMR spectroscopy. *Quart Revs Biophysics 24*:479–532.

Wimberly BT. 1992. NMR-derived structures of RNA loops: The conformation of eukaryotic 5S ribosomal loop E. Ph.D. Thesis. University of California, Berkeley.

Wyatt JR, Chastain M, Puglisi JD. 1991. Synthesis and purification of large amounts of RNA oligonucleotides. *BioTechniques 11*:764–769.